Electronic Supplementary Material (ESI) for Journal of Materials Chemistry C.

Supplementary Information

Boosting photon absorption, exciton dissociation, and photocatalytic hydrogen and oxygen evolution reactions by build-in electric fields in Janus platinum dichalcogenides

Xu Gao[1,‡], Yanqing Shen[1,‡,*], Jiajia Liu[1], Lingling Lv[1], Min Zhou[1], Zhongxiang Zhou[1], Yuanping Feng[2], Lei Shen[3,*]

[1] *School of Physics, Harbin Institute of Technology, Harbin 150001, PR China*
[2] *Department of Physics, National University of Singapore, Singapore 117551*
[3] *Department of Mechanical Engineering, National University of Singapore, Singapore 117575*

[*]Corresponding author: Yanqing Shen, E-mail: shenyanqing2004@163.com; Lei Shen, E-mail: shenlei@nus.edu.sg

Table of Content

1. Structural stability

1.1 Thermal stability

Fig. S1 shows the total energy fluctuation per atom during the molecular dynamics simulations of the Janus PtXY materials at 300 K, accompanied by the snapshots of structures after heating for 10 ps. It is seen that the fluctuation of total energy per atom stays within a cramped scale during the simulations. There are no distinguishable structure deformations or broken bonds when heating finished. Furthermore, Tao *et al.* [1] have examined the thermal stabilities of Janus PtXY at higher temperatures of 600 K and 900 K. These indicate that the Janus PtXY materials are thermally favorable.

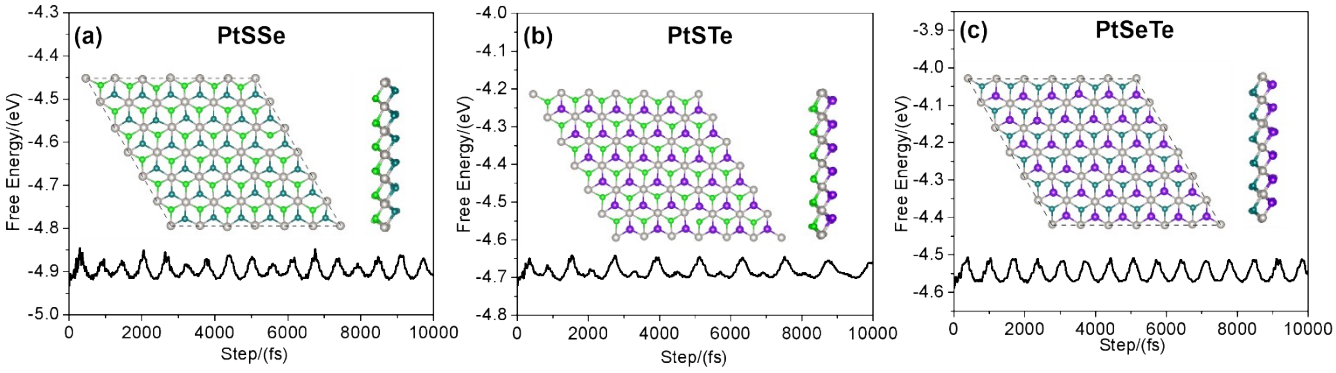

Fig. S1 The results of molecular dynamics simulations of the MLs Janus PtSSe (a), PtSTe (b) and (c) PtSeTe, with the free energy fluctuations as a function of the time step at 300 K. The grey, green, cyan and purple balls are represented for the Pt, S, Se and Te atoms, respectively.

1.2 Mechanical stability

We consider the mechanical stabilities of the ML Janus PtXY by employing the linear-elastic constants C_{ij}. It is known that for a mechanically stable 2D material, the elastic constants should obey the Born criteria [2]: $C_{11}C_{22} - C_{12}^2 > 0$, and $C_{66} > 0$. As listed in **Table S1**, we find that the criteria has been satisfied well for the ML Janus PtXY, indicative of its good mechanical stability.

Table S1 The linear-elastic coefficients C_{ij} of the ML Janus PtXY.

	C_{11} (N/m)	C_{22} (N/m)	C_{12} (N/m)	C_{66} (N/m)
PtSSe	77.72	77.72	20.61	28.73
PtSTe	65.41	65.41	17.28	24.11
PtSeTe	65.90	65.90	17.85	23.90

Table S2 Calculated lattice constants ($a = b$), thickness (h), bond length ($D_{Pt\text{-}X}$ and $D_{Pt\text{-}Y}$), the electrostatic energy difference between two surfaces ($\Delta\Phi$), dipole moment (μ) of the ML Janus PtXY (Y heavier than X), and those of the parent PtS_2, $PtSe_2$ and $PtTe_2$ based on GGA-PBE functional.

	$a = b$ (Å)	h (Å)	$D_{Pt\text{-}X}$ (Å)	$D_{Pt\text{-}Y}$ (Å)	$\Delta\Phi$ (eV)	μ (Debye)
PtS_2	3.57	2.46	2.40	2.40	-	-
$PtSe_2$	3.75	2.62	2.53	2.53	-	-
$PtTe_2$	4.02	2.78	2.71	2.71	-	-
PtSSe	3.66	2.54	2.43	2.50	0.72	0.22
PtSTe	3.81	2.62	2.50	2.63	1.52	0.48
PtSeTe	3.89	2.70	2.59	2.65	0.74	0.24

2. Band gaps of Janus PtXY

When the SOC effect is considered, the position of CBM (VBM) will be shifted downwards (upwards) by around 0.1~0.15 eV from PBE functional (see **Table S3**) and HSE06 functional [3], which provides little influence on the band edges of Janus PtXY. It is noted that the G_0W_0 calculations require expensive computational resources, thus the SOC effect is not considered in our G_0W_0 calculations.

Table S3 Corresponding electronic properties of the ML Janus PtXY, including the band gaps based on PBE functional with SOC effect ($E_{PBE}^{w/SOC}$) and without SOC effect ($E_{PBE}^{wo/SOC}$), indirect band gaps (E_{HSE06}^{i}) and direct band gaps (E_{HSE06}^{d}) at HSE06 level, indirect quasiparticle band gaps (E_{QP}^{i}) and direct quasiparticle band gaps (E_{QP}^{d}), optical band gaps (E_{opt}) using G_0W_0 + BSE method, energy positions of BGC (E_{BGC}), positions of CBM and VBM (E_{CBM} and E_{VBM}) based on E_{QP}^{i}, as well as the preliminary verification whether the materials can photocatalytically conduct overall water splitting reactions (OP), and Y and N respectively represent for can and cannot. All the results are in eV.

	$E_{PBE}^{w/SOC}$	$E_{PBE}^{wo/SOC}$	E_{HSE06}^{i}	E_{HSE06}^{d}	E_{QP}^{i}	E_{QP}^{d}	E_{opt}	E_{BGC}	E_{CBM}	E_{VBM}	OP
PtS_2	1.72	1.71	2.58	2.70	2.96	3.11	2.45	−5.51	−4.03	−6.99	Y
$PtSe_2$	1.18	1.31	1.94	2.14	2.11	2.36	1.92	−5.10	−4.05	−6.16	Y
$PtTe_2$	0.34	0.68	1.13	1.49	1.32	1.69	1.39	−4.45	−3.79	−5.11	N
PtSSe	1.33	1.47	2.21	2.35	2.43	2.58	2.02	−5.62	−4.41	−6.84	Y
PtSTe	0.71	0.86	1.50	1.86	1.66	2.04	1.59	−5.86	−5.03	−6.69	Y
PtSeTe	0.74	1.00	1.49	1.78	1.63	1.94	1.57	−5.22	−4.41	−6.04	Y

3. Solar-to-hydrogen efficiency

Assuming 100% efficiency of light absorption and carrier utilization, the STH efficiency (η_{STH}) is dependent on the light absorption efficiency (η_{abs}) and the carrier utilization efficiency (η_{cu}) of the systems, as expressed in equation S1 [4,5]:

$$\eta_{STH} = \eta_{abs} \times \eta_{cu} \tag{S1}$$

Employing the method by Yang's group [4],η_{abs} and η_{cu} can be calculated on basis of the expressions S2 and S3:

$$\eta_{abs} = \frac{\int_{E_g}^{\infty} P(h\omega)d(h\omega)}{\int_{0}^{\infty} P(h\omega)d(h\omega)} \tag{S2}$$

$$\eta_{cu} = \frac{\Delta G_{H_2O} \int_{E}^{\infty} \frac{P(h\omega)}{h\omega} d(h\omega)}{\int_{E_g}^{\infty} P(h\omega)d(h\omega)} \tag{S3}$$

where ΔG = 1.23 eV is the potential difference for water splitting, $P(h\omega)$ is the AM1.5 solar energy flux at a photon energy of $h\omega$ and E represents the energy of photons that can be actually used for water splitting. The way of selecting E is described in expression S4, and ΔE_1 and ΔE_2 are equal to χ_2 and χ_1 in our descriptions, respectively.

$$E = \begin{cases} E_g, (\Delta E_1 \geq 0.6eV, \Delta E_2 \geq 0.2eV) \\ E_g + 0.6 - \Delta E_1, (\Delta E_1 < 0.6eV, \Delta E_2 \geq 0.2eV) \\ E_g + 0.2 - \Delta E_2, (\Delta E_1 \geq 0.6eV, \Delta E_2 < 0.2eV) \\ E_g + 0.8 - \Delta E_1 - \Delta E_2, (\Delta E_1 < 0.6eV, \Delta E_2 < 0.2eV) \end{cases} \tag{S4}$$

Besides, in the above expressions, E_g is the band gap at HSE06 level. Taking the existence of $\Delta\Phi$ into consideration, the expression S5 is used to acquire the corrected STH efficiency (η'_{STH}), where ΔV is equal to $\Delta\Phi$ here. Based on the above details, the light absorption efficiency η_{abs}, carrier utilization efficiency η_{cu}, and STH efficiency η_{STH}, as well as the corrected STH efficiency η'_{STH} of ML Janus PtXY are calculated and listed in **Table S4**.

$$\eta'_{STH} = \eta_{STH} \times \frac{\int_0^{\infty} P(h\omega)d(h\omega)}{\int_0^{\infty} P(h\omega)d(h\omega) + \Delta V \int_{E_g}^{\infty} \frac{P(h\omega)}{h\omega} d(h\omega)} \quad \text{(S5)}$$

Table S4 Calculated energy conversion efficiency of light absorption (η_{abs}), carrier utilization (η_{cu}), STH (η_{STH}), and corrected STH (η'_{STH}) of the ML Janus PtXY, as well as those of Janus MXY [5] and MoS_2/WS_2.

	η_{abs} (%)	η_{cu} (%)	η_{STH} (%)	η'_{STH} (%)
PtSSe	27.9	46.0	12.8	11.9
PtSTe	61.5	57.9	35.6	24.7
PtSeTe	62.0	39.5	24.5	20.1
MoSSe	35.7	48.7	17.4	15.7
MoSTe	61.5	46.8	28.8	20.1
WSSe	29.1	31.2	9.1	8.4
WSTe	50.7	34.9	17.7	13.5
MoS_2	30.6	40.6	12.4	12.4
WS_2	24.2	24.5	5.9	5.9

* The calculated energy conversion efficiencies will be reduced in the practical applications due to the energy loss and partial recombination of electrons and holes.

For comparison, we calculate the energy conversion efficiencies of the ML Janus MXY [6] and MoS_2/WS_2. The band gaps at HSE06 level (E_{HSE06}), energy positions of BGC (E_{BGC}), positions of CBM/VBM (E_{CBM}/E_{VBM}), overpotentials for HER/OER (χ_1/χ_2) and electrostatic potential difference ($\Delta\Phi$) of ML Janus MXY and MoS_2/WS_2 are summarized in **Table S5**. The band alignments are drawn to verify whether Janus MXY and MoS_2/WS_2 are potential photocatalysts for overall water splitting, as depicted in **Fig. S2**. It is found that Janus MoSSe, MoSTe, WSSe, WSTe and MoS_2/WS_2 can proceed both HER and OER. Therefore, the energy conversion efficiencies of above six materials are calculated and shown in **Table S4**.

Table S5 Calculated HSE06 band gaps (E_{HSE06}), energy position of BGC (E_{BGC}), positions of CBM/VBM (E_{CBM}/E_{VBM}), overpotentials for HER/OER (χ_1/χ_2) and electrostatic potential difference ($\Delta\Phi$) of ML Janus MXY and MoS_2/WS_2. All values are in eV.

	E_{HSE06}	E_{BGC}	E_{CBM}	E_{VBM}	χ_1	χ_2	$\Delta\Phi$
MoSSe	2.02	−5.30	−4.29	−6.30	0.92	0.63	0.77
MoSTe	1.50	−5.35	−4.60	−6.10	1.33	0.43	1.49
MoSeTe	1.70	−4.88	−4.03	−5.63	1.13	-	0.72
WSSe	2.18	−4.95	−3.86	−6.04	1.29	0.37	0.71
WSTe	1.71	−5.11	−4.26	−5.97	1.60	0.30	1.42
WSeTe	1.80	−4.62	−3.72	−5.52	1.43	-	0.71
MoS_2	2.14	−5.11	−4.04	−6.18	0.40	0.51	-
WS_2	2.31	−4.80	−3.65	−5.96	0.79	0.29	-

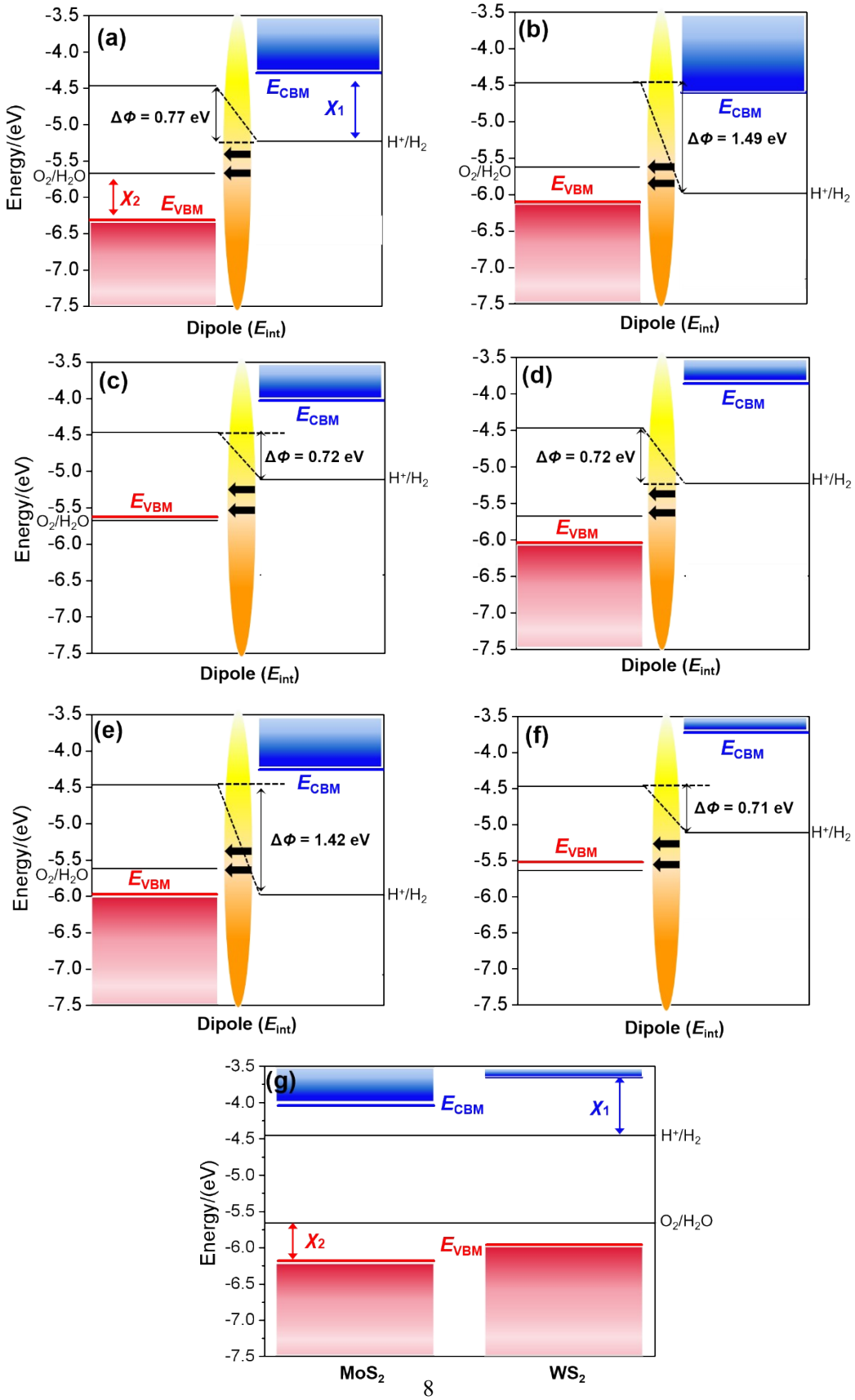
(a)
(b)
(c)
(d)
(e)
(f)
(g)
Energy/(eV)
Dipole (E_{int})
E_{CBM}
E_{VBM}
X_1
X_2
ΔΦ = 0.77 eV
ΔΦ = 1.49 eV
ΔΦ = 0.72 eV
ΔΦ = 0.72 eV
ΔΦ = 1.42 eV
ΔΦ = 0.71 eV
H^+/H_2
O_2/H_2O
MoS_2
WS_2

Fig. S2 Band alignments with regarding to the vacuum level of MLs Janus MoSSe (a), MoSTe (b), MoSeTe (c), WSSe (d), WSTe (e), WSeTe (f) and MoS_2/WS_2 (g).

Devoted to the suitable overpotential for HER χ_1 and overpotential for OER χ_2, the energy conversion efficiencies of carrier utilization are close to 40~60% for Janus PtXY. Correspondingly, the high efficiencies of both light absorption and carrier utilization together ascribe to the high STH energy conversion efficiency η_{STH} of 35.6% and 24.5% for Janus PtSTe and PtSeTe, respectively. Besides, this η_{STH} is higher than those of the bilayer C_3N_5 of 4.54% [7], bilayer $LiAlS_2$ of 9.97% [8], and Janus MoSSe, WSSe, MoSTe and WSTe of 8.4~15.7% (see **Table S4**), but a bit lower than or comparable to those of bilayers $LiAlTe_2$ and $LiGaSe_2$ of respectively 25.34 and 28.68 % [8] and ML B_2P_6 of 28.2% [9]. Strikingly, the corrected STH conversion efficiency η'_{STH} of the Janus PtSTe and PtSeTe using the full solar spectrum reaches up to 24.7% and 20.1%, respectively, higher compared with the conventional theoretical limit of 18% [10], which is attributed the success to the relatively small band gaps and good abilities to absorb more visible light for water splitting.

4. Details of band alignments

The band alignments of the Janus PtXY are simulated to study their potential for photocatalytically splitting water. The positions of CBM and VBM are defined as follows [11]:

$$E_{CBM} = E_{BGC} - \frac{1}{2}E_{QP}^{i} \tag{S6}$$

$$E_{VBM} = E_{BGC} + \frac{1}{2}E_{QP}^{i} \tag{S7}$$

where E_{BGC} is the band gap center energy with respect to the vacuum level. One advantage of this definition is that E_{BGC} is negligibly affected by the different functionals used [11]. In this work, GGA-PBE functional is used to obtain E_{BGC}.

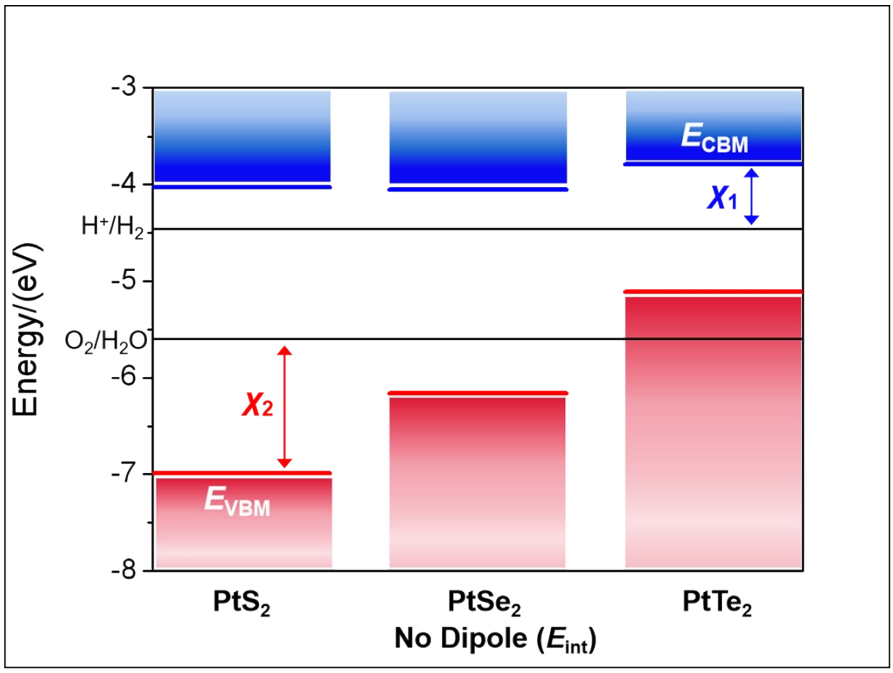

Fig. S3 Band alignments of bare ML PtX_2, where χ_1 and χ_2 represent the overpotentials for HER and OER, respectively.

5. Electrostatic potential of Janus PtXY

It is observed that in ML Janus PtSSe, the S and Se atoms both act electron acceptors of 0.22 and 0.06 *e* per unit cell, respectively, however, Pt atoms donate the electron of 0.28 *e*. Similar results can also be found for PtSTe and PtSeTe.

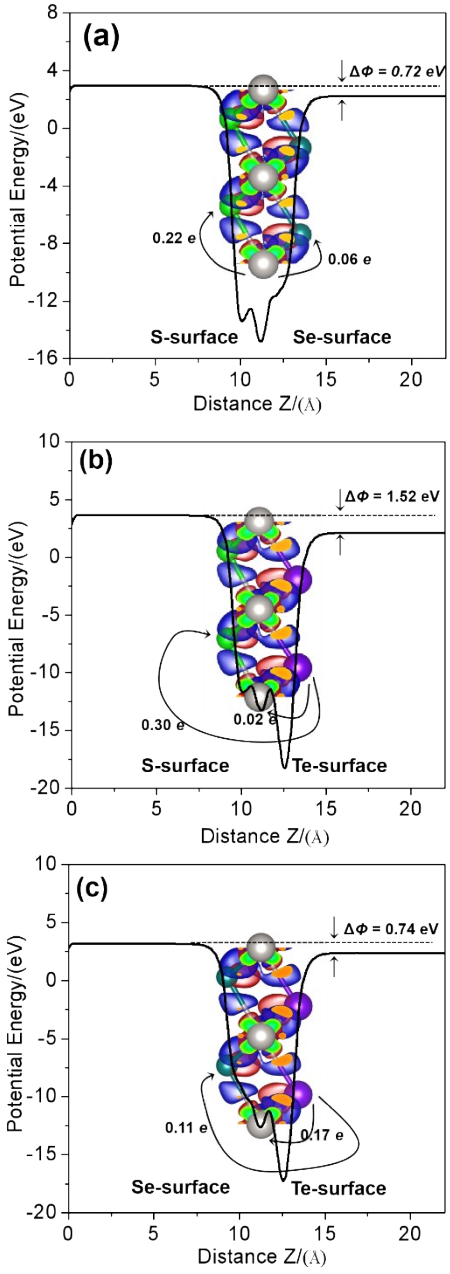

Fig. S4 Electrostatic potential illustrations along *z*-direction and the three-dimensional charge difference densities with the insets representing the Bader charge analysis per unit cell of Janus PtSSe (a), PtSTe (b) and PtSeTe (c), where the blue and red regions represent the electron accumulation and depletion, respectively. The isosurface value is 0.007 e/Å^3.

6. Exciton Binding Energy

The exciton binding energy (E_{EB}) is defined as the energy difference between the direct quasi-particle band gap from G_0W_0 calculations (E_{QP}^{d}) and the first absorption peak of dielectric imaginary part (E_{opt}) by G_0W_0 + BSE approach, as described in the following expression:

$$E_{\mathrm{EB}} = (E_{QP}^{d} - E_{\mathrm{opt}}) \tag{S8}$$

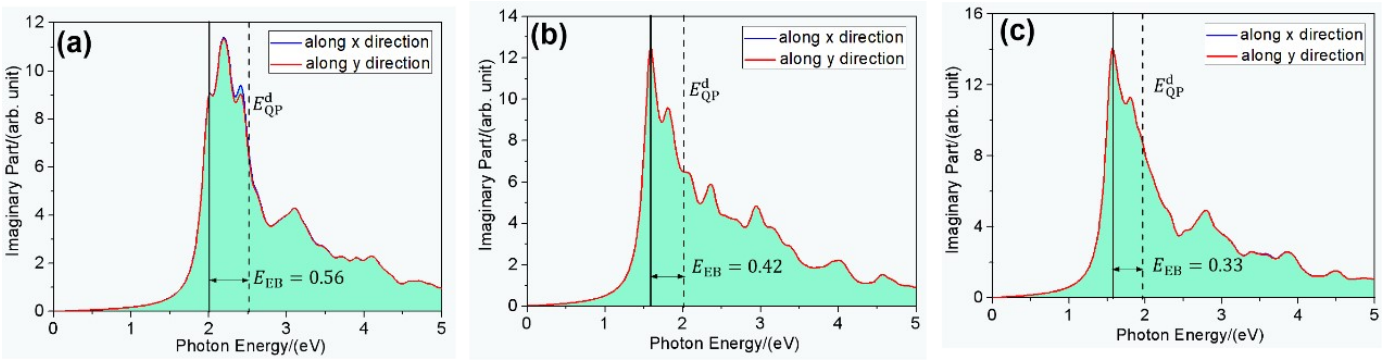

Fig. S5 The imaginary parts of dielectric functions of Janus PtSSe (a), PtSTe (b) and PtSeTe (c), indicative of the obvious isotropy for the optical response of Janus PtXY.

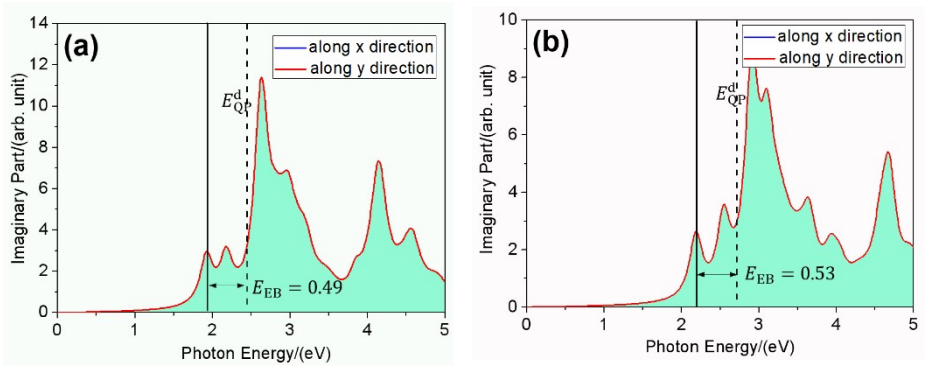

Fig. S6 The imaginary parts of dielectric functions of MoS_2 (a) and WS_2 (b). It shows that PtSTe and PtSeTe own smaller exciton binding energies compared to MoS_2 and WS_2.

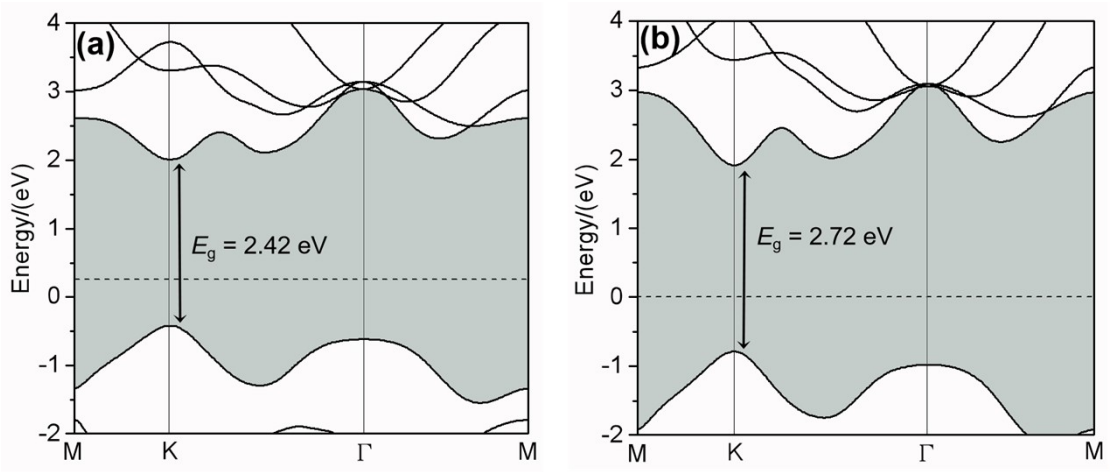

Fig. S7 G_0W_0 band structures of MoS_2 (a) and WS_2 (b). The Fermi level is set to zero level and indicated by black dashed lines. It shows that MoS_2 and WS_2 have a direct band gap of 2.42 eV and 2.72 eV, respectively. The band gaps are used to calculate the exciton binding energy combined with **Fig. S6**.

7. Carrier mobility

We calculate the carrier mobility of Janus PtXY via the following equation based on the deformation potential theory (DPT) [12]:

$$\mu = \frac{2eh^3 C_{2D}}{3K_B T \left|m^*\right|^2 E_d^2} \tag{S9}$$

where the carrier mobility μ_{2D} depends on the elastic modulus C_{2D}, effective mass m^*, and deformation potential constant E_d. In addition, e, $\hbar$, k_B, and T are the electron charge, reduced Planck constant, Boltzmann constant, and the temperature is set at 298.15 K. Herein, the elastic modulus C_{2D} is defined as $C_{2D} = \left(\partial^2 E / \partial \varepsilon^2\right) / S_0$, where E is the total energy and S_0 is the equilibrium area of the optimized 2D structure. The carrier effective mass m^* is obtained using $m^* = \pm h^2 \left(\mathrm{d}^2 E_k / \mathrm{d}k^2\right)^{-1}$. The deformation potential constant E_d is derived from $E_d = \partial E_{edge} / \partial \varepsilon$, where E_{edge} is the band edge energy of the CBM for electrons and VBM for holes induced by the strain ε.

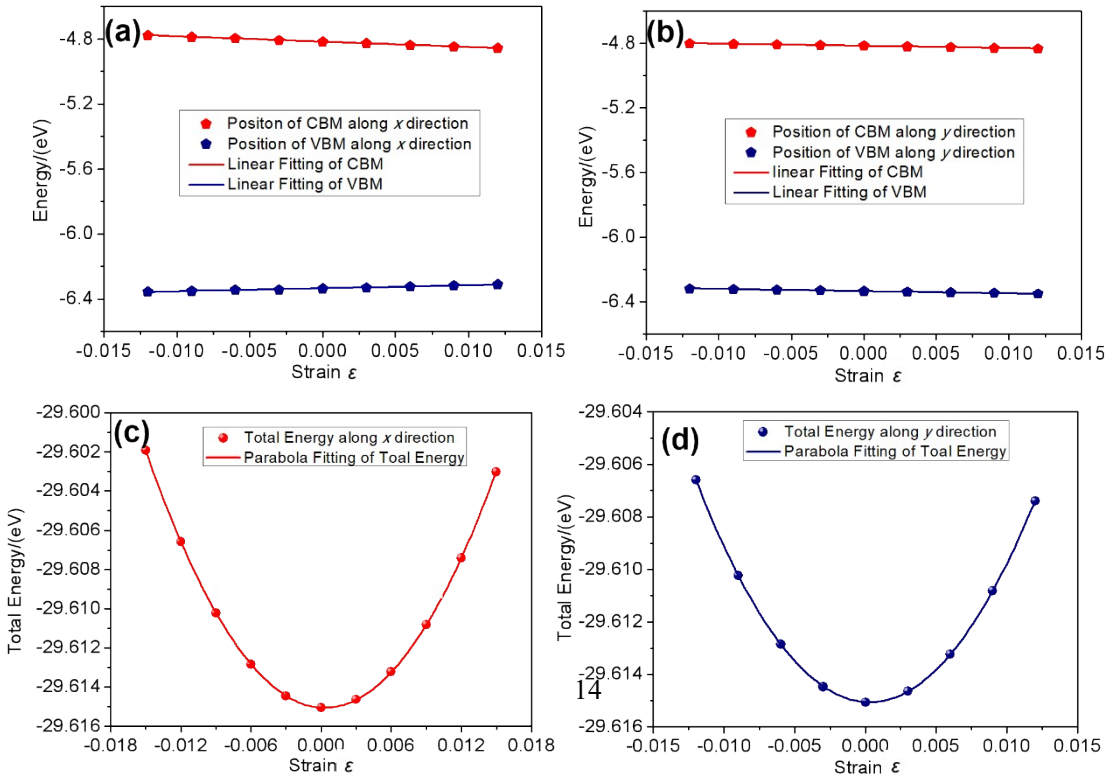

Fig. S8 Evolution of energy positions of CBM and VBM with respect to the vacuum level when uniaxial strains are employed along the *x* direction (a) and *y* direction (b) of Janus PtSSe. Total energy of Janus PtSSe in rectangular unit cell as a function of the applied uniaxial strains along *x* direction (c) and *y* direction (d).

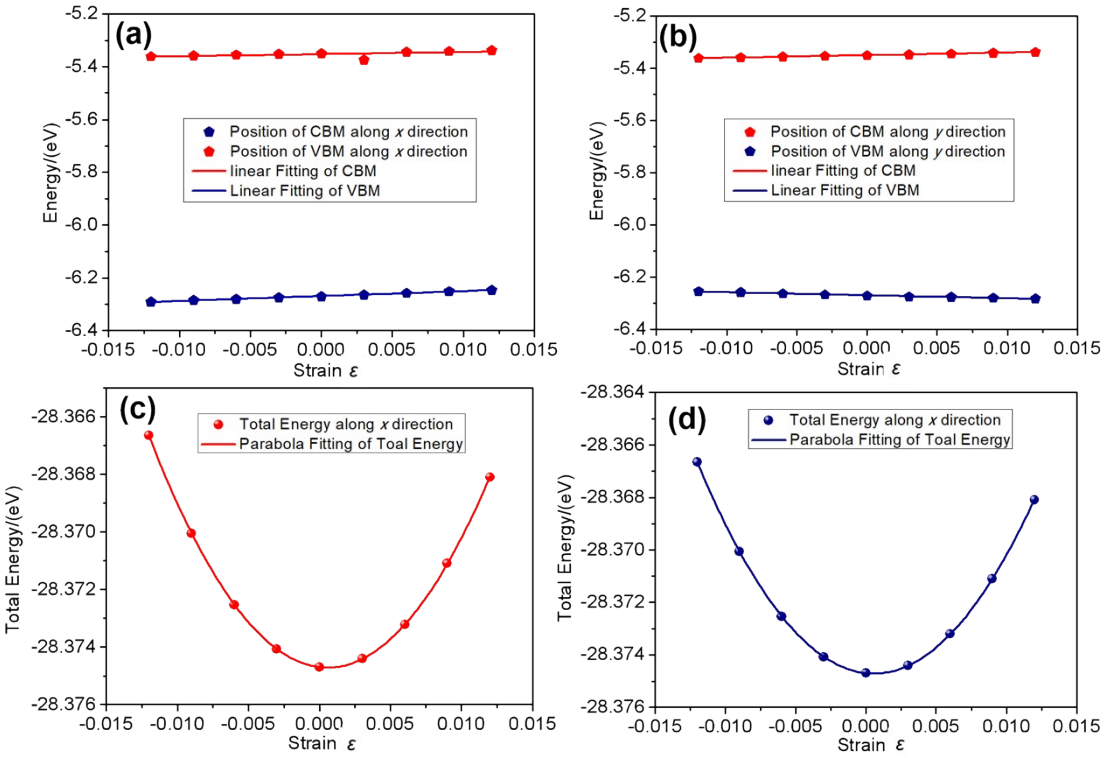

Fig. S9 Evolution of energy positions of CBM and VBM with respect to the vacuum level when uniaxial strains are employed along the *x* direction (a) and *y* direction (b) of Janus PtSTe. Total energy of Janus PtSTe in rectangular unit cell as a function of the applied uniaxial strains along *x* direction (c) and *y* direction (d).

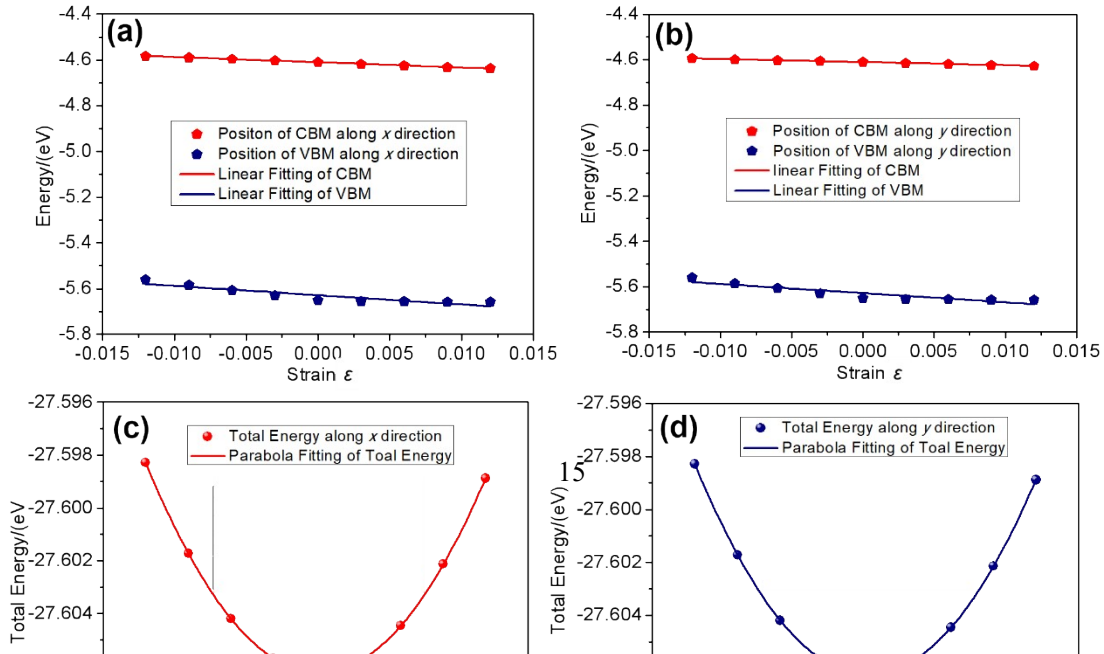

Fig. S10 Evolution of energy positions of CBM and VBM with respect to the vacuum level when uniaxial strains are employed along the *x* direction (a) and *y* direction (b) of Janus PtSeTe. Total energy of Janus PtSeTe in rectangular unit cell as a function of the applied uniaxial strains along *x* direction (c) and *y* direction (d).

Table S6 Elastic modulus (C_{2D}), effective mass (m^*), deformation potential (E_d) and carrier mobility (μ_{2D}) of Janus PtXY along *x* and *y* directions.

	Carrier type		C_{2D} (N m^{-1})	m^*	E_d (eV)	μ_{2D} (cm^2 V^{-1} s^{-1})
PtSSe	Electrons	*x*	77.27	0.28	3.30	1287.06
		y	77.24	0.60	1.30	1805.45
	Holes	*x*	77.27	1.36	1.90	164.57
		y	77.24	3.47	1.33	51.57
PtSTe	Electrons	*x*	64.9	1.05	0.80	1308.03
		y	64.9	0.81	0.97	1495.08
	Holes	*x*	64.9	0.84	1.86	378.09
		y	64.9	0.99	1.17	687.91
PtSeTe	Electrons	*x*	64.9	0.16	2.29	6874.89
		y	64.9	0.18	1.38	14957.94
	Holes	*x*	64.9	2.96	4.05	6.42
		y	64.9	3.38	4.04	4.95

8. Adsorption of water molecule

Table S7 The calculated adsorption energies (E_{ads}) of H_2O molecule on the different surfaces of the Janus PtXY and the vertical distances between surfaces of PtXY and the H_2O molecule (D).

		E_{ads}/(eV)	D/Å
PtSSe	S-surface	−0.232	2.19
	Se-surface	−0.208	2.63
PtSTe	S-surface	−0.256	2.16
	Te-surface	−0.223	2.65
PtSeTe	Se-surface	−0.246	2.23
	Te-surface	−0.233	2.58

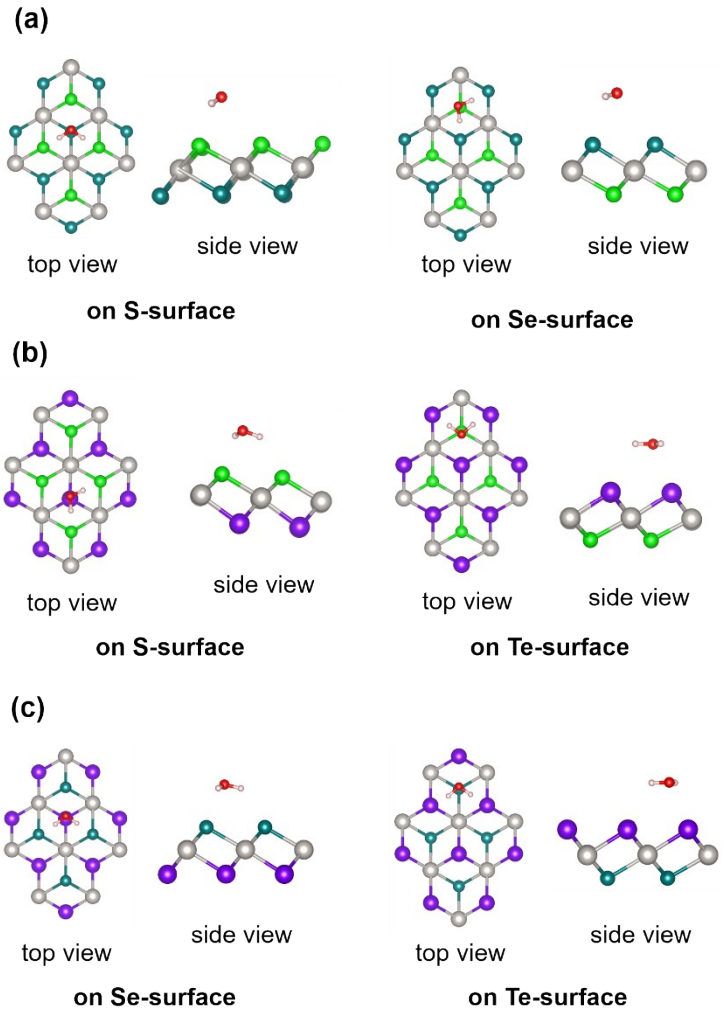

Fig. S11 The stable configurations with H_2O adsorption on the Janus PtSSe (a), PtSTe (b) and PtSeTe (c).

9. Gibbs free energy

At pH = 0, the Gibbs free energy difference (ΔG) from one step to next step involved in the photocatalytic redox reactions without the light irradiation can be defined as below [13]:

$$\Delta G = \Delta E + \Delta E_{ZPE} - T\Delta S \tag{S10}$$

The complex four-step OER process is considered herein, which are presented step by step as follows:

$$* + H_2O \rightarrow OH* + H^+ + e^- \tag{S11}$$

$$OH* \rightarrow O* + H^+ + e^- \tag{S12}$$

$$O* + H_2O \rightarrow OOH* + H^+ + e^- \tag{S13}$$

$$OOH* \rightarrow * + O_2 + H^+ + e^- \tag{S14}$$

As for the HER process, it can be described in the following steps:

$$* + H^+ + e^- \rightarrow H* \tag{S15}$$

$$H* + H^+ + e^- \rightarrow * + H_2 \tag{S16}$$

where * represents the substrate materials for the adsorptions (*i.e.*, Janus PtXY), and O*, OH*, OOH* and H* represent the adsorbed intermediates during the redox reactions.

The Gibbs free energy difference of each step included in the OER and HER processes is available based on the following expressions, in which the impact of external potential and pH is taken into account:

$$\Delta G_1 = G_{OH^*} + \frac{1}{2}G_{H_2} - G_{H_2O} - G_* + \Delta G_U - \Delta G_{pH} \tag{S17}$$

(S18)

$$\Delta G_2 = G_{O^*} + \frac{1}{2}G_{H_2} - G_{OH^*} + \Delta G_U - \Delta G_{pH} \tag{S19}$$

$$\Delta G_3 = G_{OOH^*} + \frac{1}{2}G_{H_2} - G_{O^*} - G_{H_2O} + \Delta G_U - \Delta G_{pH}$$

$$\Delta G_4 = G_* + G_{O_2} + \frac{1}{2}G_{H_2} - G_{OOH^*} + \Delta G_U - \Delta G_{pH} \quad \text{(S20)}$$

$$\Delta G_5 = G_{H^*} - G_* - \frac{1}{2}G_{H_2} + \Delta G_U + \Delta G_{pH} \quad \text{(S21)}$$

$$\Delta G_6 = G_* + \frac{1}{2}G_{H_2} - G_{H^*} + \Delta G_U + \Delta G_{pH} \quad \text{(S22)}$$

For the values of U_h (U_e) at pH = 0, taking PtSSe as an example, the energy position of VBM (CBM) is −6.84 (−4.41) eV (see Table S3), and U_h (U_e) is defined as the energy difference between the VBM (CBM) and the reduction potential (−4.44 eV), thus U_h = −4.44 – (–6.84) = 2.40 V, U_e = (−4.41) − (−4.44 – 0.72) = 0.75 V for PtSSe, and the values of U_h (U_e) of PtSTe and PtSeTe can be obtained using the similar method.

The external potentials provided by the photogenerated electrons and holes between pH = 0 and pH ≠ 0 can be written in the following equations [14,15]:

$$U_e^{pH} = U_e^{pH=0} - \text{pH} \times 0.059 \quad \text{(S23)}$$

$$U_h^{pH} = U_h^{pH=0} + \text{pH} \times 0.059 \quad \text{(S24)}$$

From **Table S3** and **Fig. 3**, $U_h^{pH=0}(U_h^{pH=7})$ of ML Janus PtSSe is 2.40 (2.82) V. Correspondingly, the $U_e^{pH=0}$ ($U_e^{pH=7}$) of the ML Janus PtSSe is 0.75 (0.33) V. Using the same method, $U_h^{pH=0}(U_h^{pH=7})$ and $U_e^{pH=0}(U_e^{pH=7})$ provided by the photogenerated holes and electrons of the MLs Janus PtSTe and PtSeTe are calculated to be 2.25 (2.67) and 0.93 (0.51) V, and 1.60 (2.02) and 0.77 (0.35) V, respectively.

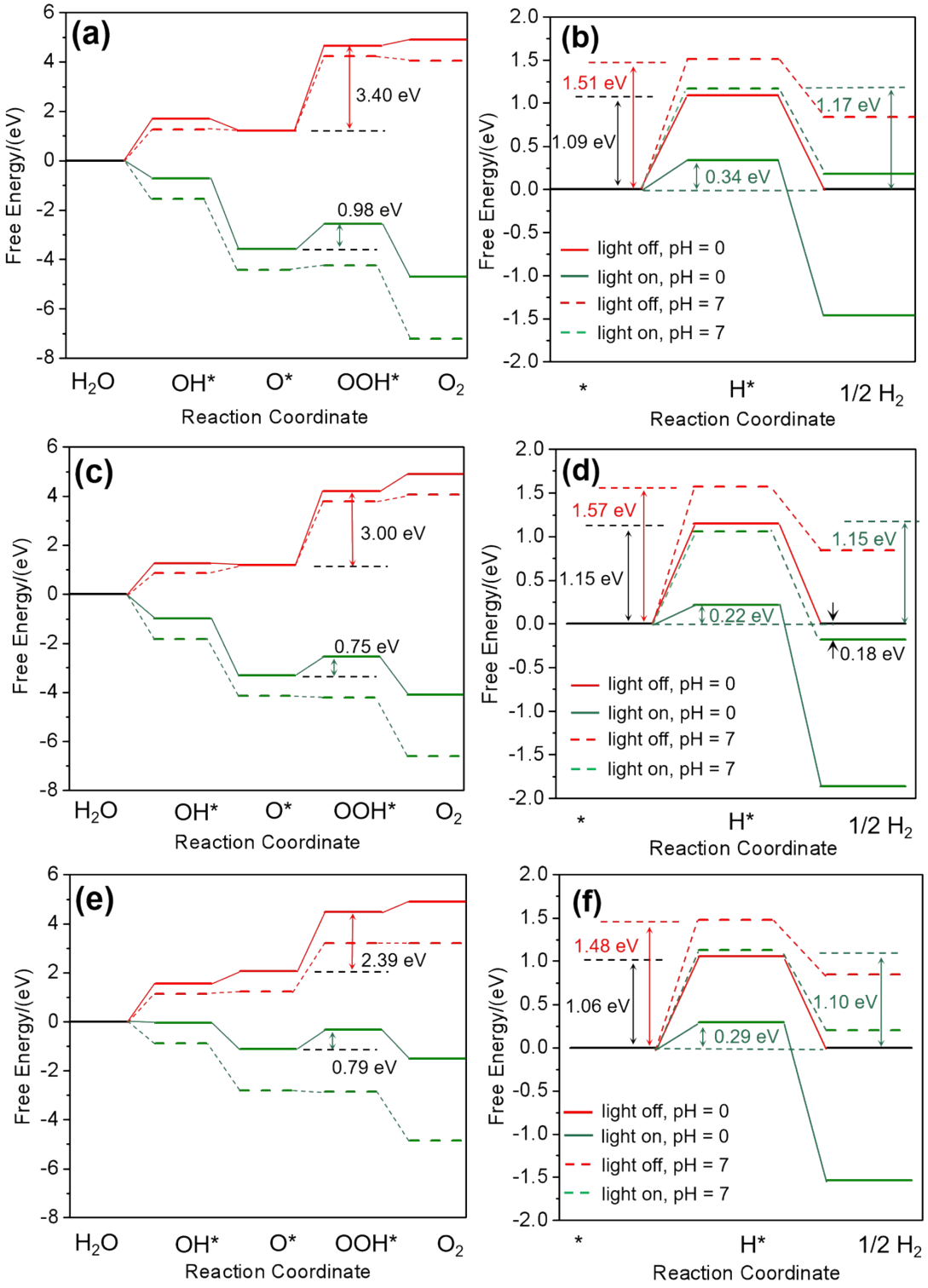

Fig. S12 Comparison of free energy steps of OER and HER processes at pH = 0 and pH = 7 on the MLs Janus PtSSe (a-b), PtSTe (c-d) and PtSeTe (e-f).

10. Theoretical calculation models

A hybrid exchange–correlation functional is usually constructed as a linear combination of the Hartree–Fock exact exchange functional and any number of exchange and correlation explicit density functionals.

$$E_{\mathrm{x}}^{\mathrm{HF}}=-\frac{1}{2}\sum_{i,j}\iint\psi_i^*\left(\mathbf{r}_1\right)\psi_j^*\left(\mathbf{r}_2\right)\frac{1}{r_{12}}\psi_j\left(\mathbf{r}_1\right)\psi_i\left(\mathbf{r}_2\right)d\mathbf{r}_1d\mathbf{r}_2 \tag{1}$$

The HSE (Heyd–Scuseria–Ernzerhof) exchange–correlation functional uses an error-function-screened Coulomb potential to calculate the exchange portion of the energy in order to improve computational efficiency, especially for metallic systems:

$$E_{\mathrm{xc}}^{\omega\mathrm{PBEh}}=aE_{\mathrm{x}}^{\mathrm{HF,SR}}(\omega)+(1-a)E_{\mathrm{x}}^{\mathrm{PBE,SR}}(\omega)+E_{\mathrm{x}}^{\mathrm{PBE,LR}}(\omega)+E_{\mathrm{c}}^{\mathrm{PBE}} \tag{2}$$

where α is the mixing parameter, and ω is an adjustable parameter controlling the short-rangeness of the interaction. Standard values of α = 1/4 and ω = 0.2 (usually referred as to HSE06) have been shown to give good results for most systems. $E_{x}^{HF,SR}(\omega)$ is the short-range Hartree–Fock exact exchange functional, $E_{x}^{PBE,SR}(\omega)$ and $E_{x}^{PBE,LR}(\omega)$ are the short- and long-range components of the PBE exchange functional, and $E_{c}^{PBE}(\omega)$ is the PBE correlation functional.

As for the GW method [16], employing the energies ϵ_{n} and the orbitals ϕ_{n}, which solve the Kohn-Sham equations of DFT, an initial Green's function $G^{(0)}$ can be constructed [17,18]:

$$G_0\left(\mathbf{r},\mathbf{r}',z\right)=\sum_{n=1}^{N}\frac{\phi_n(\mathbf{r})\overline{\phi}_n\left(\mathbf{r}'\right)}{z-\epsilon_n+\mathrm{i}\,\eta\,\mathrm{sgn}\left(\epsilon_n-\mu\right)} \tag{3}$$

The self-energy in G_0W_0 reads:

$$\hat{\Sigma}_{G_0W_0}(12)=\mathrm{i}G_0\left(12^+\right)W_0\left(12^+\right) \tag{4}$$

A representation in energy space is employed by performing a Fourier transformation:

$$\hat{\Sigma}_{G_0W_0}\left(\mathbf{r},\mathbf{r}',z\right)=\frac{i}{2\pi}\int\mathrm{d}E'G_0\left(\mathbf{r},\mathbf{r}',z-E'\right)W_0\left(\mathbf{r},\mathbf{r}',E'\right)e^{(-i\delta E')} \tag{5}$$

From this self-energy, the external potential $\hat{V}_{ext}$ from the ions, and the Hartree potential

$\hat{V}_{\mathrm{H}}[G_0]$ an energy-dependent non-interacting effective potential $V_{\mathrm{GW}}(z)$ is constructed as follows:

$$V_{GW}(z) = V_{\mathrm{ext}} + V_{\mathrm{H}}[G_0] + \Sigma(z) \tag{6}$$

The potential $\hat{V}_{\mathrm{H}}[G_0]$ is calculated from the electron density of G_0, respectively the underlying non-interacting system. With the potential $V_{\mathrm{GW}}(z)$ the G_0W_0 approach can be understood as a prescript which generates an energy dependent perturbative correction $\Delta V(z)$ to the exchange-correlation potential $\hat{V}_{\mathrm{xc}}$ from DFT given by:

$$\Delta V(z) = \Sigma(z) - \hat{V}_{\mathrm{xc}} \tag{7}$$

Employing this result, the one-body G_0W_0 Green's function $G_{G_0W_0}$ is given as:

$$G^{-1}_{G_0W_0}(z) = E - H_{G_0W_0}(z) \tag{8}$$

with：

$$H_{G_0W_0}(z) = -\frac{\nabla^2}{2m} + V_{GW}(z) \tag{9}$$

$$= -\frac{\nabla^2}{2m} + V_{\mathrm{H}} + V_{\mathrm{ext}} + \Sigma(z) \tag{10}$$

$$= -\frac{\nabla^2}{2m} + V_{\mathrm{H}} + V_{\mathrm{ext}} + \hat{V}_{\mathrm{xc}} + \Delta V(z) \tag{11}$$

The pole positions of $G_{G_0W_0}$ respectively the QP-energies ϵ_{n}' are found as solutions of the QP-equation:

$$\left(H_{G_0W_0}(\varepsilon_{n'}) - \varepsilon_{n'}\right)|\psi_n\rangle = 0 \tag{12}$$

with the QP-orbitals $|\psi_{\mathrm{n}}\rangle$.

In a simpler flavor of G_0W_0, one approximates the QP-orbitals with Kohn-Sham sates $\psi_{\mathrm{n}} \approx \phi_{\mathrm{n}}$. In this spirit, all off-diagonal elements in the QP-equation Eq. (12) are neglected and the QP-energies are calculated from:

$$\varepsilon_{n'} \approx \langle\phi_n| -\frac{\nabla^2}{2m} + V_{\mathrm{ext}} + V_{\mathrm{H}} + \hat{V}_{\mathrm{xc}} + \Delta V(\varepsilon_{n'})|\phi_n\rangle \tag{13}$$

$$= \langle\phi_n| -\frac{\nabla^2}{2m} + V_{\mathrm{ext}} + V_{\mathrm{H}} + \hat{V}_{\mathrm{xc}}|\phi_n\rangle + \langle\phi_n|\Sigma(\varepsilon_{n'}) - \hat{V}_{\mathrm{xc}}|\phi_n\rangle \tag{14}$$

$$= \dot{\phi}_n + \langle\phi_n|\Sigma(\varepsilon_{n'}) - \hat{V}_{\mathrm{xc}}|\phi_n\rangle \tag{15}$$

with the Kohn-Sham energies ϵ_n and the perturbative G_0W_0 correction from (7) which is given for each single energy by the matrix element $\langle \phi_n | \Sigma(\varepsilon_{n'}) - \hat{V}_{xc} | \phi_n \rangle$.

References

[1] W. L. Tao, J. Q. Lan, C. E. Hu, Y. Cheng, J. Zhu and H. Y. Geng, *J. Appl. Phys.*, 2020, **127,** 035101.

[2] M. Born and K. Huang, Dynamical Theory of Crystal Lattices; Clarendon Press. 1954.

[3] F. Ersan and C. Ataca, *Phys. Rev. Appl.*, 2020, **13**, 064008.

[4] C. F. Fu, J. Y. Sun, Q. Q. Luo, X. X. Li, W. Hu and J. L. Yang, *Nano Lett.*, 2018, **18**, 6312−6317.

[5] Q. K. Yin, C. L. Yang, M. S. Wang and X. G. Ma, *J. Mater. Chem. C*, 2021, DOI: 10.1039/d1tc02423j.

[6] C. X. Xia, W. Q. Xiong, J. Du, T. X. Wang, Y. T. Peng and J. B. Li, *Phys. Rev. B*, 2018, **98**, 165424.

[7] S. Y. Qi, Y. C. Fan, J. R. Wang, X. H. Song, W. F. Li and M. W. Zhao, *Nanoscale*, 2020, **12**, 310.

[8] Y. C. Fan, X. H. Song, S. Y. Qi, X. K. Ma and M. W. Zhao, *J. Mater. Chem. A*, 2019, **7**, 26123.

[9] M. L. Sun and U. Schwingenschlögl, *Chem. Mater.*, 2020, **32**, 4795−4800.

[10] M. G. Walter, E. L. Warren, J. R. McKone, S. W. Boettcher, Q. Mi, E. A. Santori and N. S. Lewis, *Chem. Rev.*, 2010, **110**, 6446−6473.

[11] M. C. Toroker, D. K. Kanan, N. Alidoust, L. Y. Isseroff, P. Liao and E. A. Carter, *Phys. Chem. Chem. Phys.*, 2011, **13**, 16644−16654.

[12] J. Bardeen and W. Shockley, *Phys. Rev.*, 1950, **80**, 72−80.

[13] J. K. Nørskov, J. Rossmeisl, A. Logadottir and L. Lindqvist, *J. Phys. Chem. B*, 2004, **108**, 17886−17892.

[14] L. Ju, M. Bie, X. Tang, J. Shang and L. Z. Kou, *ACS Appl. Mater. Interfaces*, 2020, **12**, 29337–29338.

[15] C. F. Fu, Q .Q. Luo, X. X. Li and J. L. Yang, *J. Mater. Chem. A*, 2016, **4**, 18892−18898.

[16] M. S. Hybertsen and S. G. Louie, *Phys. Rev. B*, 1986, **34**, 5390–5413.

[17] R. W. Godby, M. Schluter and L.J. Sham, *Phys. Rev. B*, 1988, **37**, 10159–10175.

[18] Rer. Nat. Quasiparticle self-consistent GW-approximation for molecules: [D]. Baden Wuertenberg: Karlsruhe Institute of Technology, 2015.